International Journal of Heat and Mass Transfer 127 (2018) 813–828

Contents lists available at ScienceDirect

International Journal of Heat and Mass Transfer

journal homepage: www.elsevier.com/locate/ijhmt

Two-phase frictional pressure drop and water film thickness in a thin hydrophilic microchannel

James M. Lewis, Yun Wang *

Renewable Energy Resources Laboratory, National Fuel Cell Research Center, and Department of Mechanical and Aerospace Engineering, University of California, Irvine, CA, United States

ARTICLE INFO

Article history:
Received 5 February 2018
Received in revised form 21 May 2018
Accepted 14 August 2018
Available online 25 August 2018

Keywords:
Two-phase flow
Air-water
Frictional pressure drop
Water film thickness
Microchannel

ABSTRACT

This study focuses on the experimental investigation of the two-phase pressure drop and water film thickness in a thin microchannel. Air-water flow in the thin channel of dimensions 3.23 mm wide by 0.304 mm high produces a stratified flow over a range of test conditions. The experimental data allowed for the assessment of several models including homogeneous, separated, and relative permeability models. A comparison of the two-phase pressure to the recently developed two-fluid model (Wang, 2009) resulted in a new exponent (n_k) of 1.159 for the relative permeability, which produced a mean absolute percent error of 3.25%. Imaging of the air-water flow allowed for measuring the water film thickness, which showed good agreement with the analytical solution of Steinbrenner (2011) and the two-fluid model with a mean error of −0.035. The study demonstrates the applicability for the two-fluid model to predict both the two-phase pressure and the water film thickness in thin microchannels.

Published by Elsevier Ltd.

1. Introduction

Two-phase flow in thin microchannels has become ubiquitous in modern engineering and found in lab-on-chips, PEM (Polymer Electrolyte Membrane) fuel cells, micro-heat pipes, and heat exchangers. In PEM fuel cells, gas supply channels have a cross-section dimension at the micro/millimeter scale and a length scale of one to tens of centimeters. Not only do the gas channels supply air, the channels serve to remove water generated by the oxygen reduction reaction occurring at the cathode catalyst layer that could potentially cause severe flooding [38,37]. The two-phase pressure drop and water content in the channel act as indicators to flooding.

While computational methods exist to study two-phase flows, such as volume-of-fluid (VOF), the level-set method, and the Lattice-Boltzmann Method (LBM), experimentation and semi-empirical models reinforce the numerical results. Researchers have proposed many different semi-empirical models to determine the two-phase pressure drop which typically fall into one of three categories: homogeneous flow, separated flow, and relative permeability models. The homogeneous flow model treats the two-phase flow as an equivalent single-phase flow by averaging the two fluid properties together, particularly the viscosity. Through dynamic similarity Dukler et al. [10] weighted the viscosity based on the ratio of the liquid volumetric flow rate to the total volumetric flow rate. The model predicted the experimental data for two-component flows in tubes of diameter 2.54–12.7 cm (1–5 in.) over a range of viscosities to within −19% to 16%.

The separated flow models follow the work of Lockhart and Martinelli [21] and Chisholm [6], accounting for the interaction of the two phases through Chisholm's parameter, *C*. Lee and Lee [17] conducted experiments in horizontal channels of 20 mm width and 0.4, 1, 2, and 4 mm heights. The authors found that *C* should depend on the liquid-only Reynolds number, the Capillary number, and the liquid-only Suratman number. The model predicted the experimental data within ±10%. Kim and Mudawar [16] arrived at a similar relation to Lee and Lee [17] when correlating a database of adiabatic and condensing flow experiments consisting of 17 different working fluids in tubes/channels of hydraulic diameters between 0.0695 and 6.2 mm. The model predicted the experimental database with a mean absolute percent error of 23.3%.

The relative permeability models use Dary's equations to determine the two-phase pressure by modeling the form of the relative permeability in terms of the liquid saturation. For the X-model, based on the experimental work of Romm [28], the relative permeability linearly varies with the saturation such that the sum of gas and liquid relative permeabilities equal 1. Conversely, Corey [9] investigated oil-gas flows in conventional tubes and showed that the liquid relative permeability equals the liquid saturation raised

* Corresponding author.
E-mail address: yunw@uci.edu (Y. Wang).

https://doi.org/10.1016/j.ijheatmasstransfer.2018.08.060
0017-9310/Published by Elsevier Ltd.

to the power of 4. This correlated two-thirds of Corey's experimental data well. In general, the relative permeability exponent varies between 1 and 4.

Though various models for the two-phase pressure exist that can accurately predict the two-phase pressure, the models rely on multiple correlation parameters. Wang [36] proposed the two-fluid model to investigate the porous channels in PEM fuel cells, treating the gas flow channels as porous media. Unlike other relative permeability models that require the experimental measurement of the saturation, the two-fluid model poses a model for the saturation. Thus, the use of the two-fluid model requires only a single correlation parameter, the relative permeability exponent n_k. Adroher and Wang [1] and Cho and Wang [7] showed the applicability of the model to standard gas flow channels in PEM fuel cells. In a channel of 1.6 mm wide by 1 mm high, Adroher and Wang [1] found an n_k value of 2 only resulted in a qualitative agreement between the experimentally measured two-phase pressure drop for superficial gas velocities in the range of 5–10 m/s. Cho and Wang [7] applied the two-fluid model to both hydrophilic and hydrophobic channels of dimensions 1.68 mm wide by 1.00 mm high by 150 mm long. The authors found that n_k values varied with flow pattern but remain a constant value of 2.49, 2.15, and 1.96 for slug, wavy, and annulus flow patterns, respectively. However, the two-fluid model has not been applied to thin microchannels nor has the model's ability to predict water film thickness been tested.

Through an experimental study, this work seeks to demonstrate the applicability of the two-fluid model in the common flow range of operational PEM fuel cells for thin microchannels. In addition to selected existing models, Section 2 introduces the two fluid model. The analytical solution to stratified flow proposed in dimensionless form by Steinbrenner [33] used for comparison to the optically measured water film thickness follows in Section 3. Section 4 details the experimental apparatus to produce air-water flow in a 3.23 mm wide by 0.304 mm high by 164 mm long microchannel and the testing method. Finally, Section 5 discusses the validation of the experimental setup and the assessment of existing models. Section 5.4 discusses the new relative permeability exponent and its validation in predicting the experimental two-phase pressure and water film thickness measurements.

2. Two-phase pressure drop models

Multiple mechanisms contribute to the overall two-phase pressure drop (ΔP_{tp}) [16]:

$$\Delta P_{tp} = \Delta P_F + \Delta P_g + \Delta P_A + \Delta P_{loss} \tag{1}$$

where ΔP refers to pressure drop and the subscripts F, g, A, and *loss* refer to frictional, gravitational, acceleration, and loss, respectively. The models in this section refer only to the frictional pressure drop. The current study focuses on the adiabatic flow of air and water in a horizontal microchannel. Under adiabatic conditions, the flow will not accelerate and ΔP_A equals zero. With the channel aligned horizontally, the gravitational pressure loss also equals zero. The experimental technique seeks to minimize losses caused by entrance/exit effects and thus the loss term equals zero. This leaves that the two-phase pressure equals the two-phase frictional pressure loss.

2.1. Homogeneous flow model

The homogeneous flow model treats the two-phase flow as an equivalent single-phase flow with weighted properties under the condition that the two phases move with the same velocity. The two-phase pressure drop would thus follow:

$$\left(\frac{dP}{dz}\right)_{tp} = f_{tp}\frac{G^2}{2D_H\rho_{tp}} \tag{2}$$

where P equals the pressure, z the downstream coordinate, f the Darcy friction factor, G the total mass flux, D_H the hydraulic diameter, and ρ the density. The subscript *tp* stands for two-phase. The total mass flux (G) equals

$$G = \frac{\rho_G Q_G + \rho_L Q_L}{A_c} \tag{3}$$

where A_c stands for the cross-sectional area and Q the volumetric flow rate. The subscripts G and L stand for gas-phase and liquid-phase, respectively. The friction factor follows the standard definition for laminar flow:

$$f_{tp} = \frac{\overline{C}}{Re_{tp}} \tag{4}$$

where the correlation constant ($\overline{C}$) equals its single-phase equivalent but the Reynolds number becomes the two-phase Reynolds number (Re_{tp}) defined as:

$$Re_{tp} = \frac{GD_H}{\mu_{tp}} \tag{5}$$

Therefore, determination of the two-phase pressure drop only requires knowledge of the two-phase density (ρ_{tp}) and the two-phase dynamic viscosity (μ_{tp}). Researchers often agree that the two-phase density has the form:

$$\rho_{tp} = \left(\frac{\chi}{\rho_G} + \frac{1-\chi}{\rho_L}\right)^{-1} \tag{6}$$

where χ represents the gas quality defined as:

$$\chi = \frac{\rho_G Q_G}{\rho_G Q_G + \rho_L Q_L} \tag{7}$$

Table 1
Viscosity models for the homogeneous flow model.

Reference	Viscosity model	Test conditions
McAdams et al. [24]	$\frac{1}{\mu_{tp}} = \frac{\chi}{\mu_G} + \frac{1-\chi}{\mu_L}$	Benzene-oil, 2.69 cm tubes
Cicchitti et al. [8]	$\mu_{tp} = \mu_G\chi + (1-\chi)\mu_L$	Steam-water, 0.51 cm tubes
Lin et al. [20]	$\mu_{tp} = \frac{\mu_L\mu_G}{\mu_G + \chi^{1.4}(\mu_L - \mu_G)}$	R-12, 1 mm tubes
Dukler et al. [10]	$\mu_{tp} = \mu_L\lambda + \mu_G(1-\lambda)$	Two-component, 2.54–12.7 cm tubes
Fourar and Bories [12]	$\mu_{tp} = \lambda\mu_L + (1-\lambda)\mu_G + \sqrt{\lambda(1-\lambda)\mu_g\mu_L}$	Fractures, 0.18–1 mm gaps
Beattie and Whalley [3]	$\mu_{tp} = \mu_L(1-\beta)(1+2.5\beta)\mu_G\beta$	Multiple fluids
Awad and Muzychka [2]	$\mu_{tp} = \mu_G\frac{2\mu_G+\mu_L-2(\mu_G-\mu_L)(1-\chi)}{2\mu_G+\mu_L+(\mu_G-\mu_L)(1-\chi)}$	Refrigerants; 2.46, 2.58 mm tubes; 0.148, 1.44 mm channels
where	$\lambda = Q_L/(Q_L+Q_G)$	
	$\beta = \frac{\rho_L\chi}{\rho_L\chi+\rho_G(1-\chi)}$	

Table 2
Correlations producing a constant C-value for the separated flow model.

Reference	C Correlation	Test Conditions
Mishima and Hibiki [25]	$C = 21(1 - e^{-0.319D_H})$	Air-water, 1.07–5.00 mm gaps
Zhang et al. [39]	$C = 21\left(1 - e^{-\frac{0.674}{N_{conf}}}\right)$	$Re_G < 2000, Re_L < 2000$
English and Kandlikar [11]	$C = 5(1 - e^{-0.319D_H})$	Air-water, 1.124 mm × 0.93 mm
Li and Wu [18]	$C = 11.9Bo^{0.45}$	$Bo < 1.5$

However, researchers have proposed several forms for the two-phase viscosity, shown in Table 1.

2.2. Separated flow model

While the homogeneous model treats a two-phase flow as an equivalent single phase flow, the separated flow model seeks to account for how the interaction between the two phases influences the pressure drop. Martinelli et al. [23] determined that the two-phase pressure drop varies depending on the flow mechanism—laminar (l) or turbulent (t)—of each phase. Since the phases have different flow rates, four possible combinations exist: l-l, t-t, l-t, and t-l liquid-gas flow. Testing various liquids in air flow, Martinelli et al. [23] determined the two-phase pressure change over a change of length (L) should equal:

$$\left(\frac{\Delta P}{\Delta L}\right)_{tp} = \phi_G^2 \left(\frac{\Delta P}{\Delta L}\right)_G \tag{8}$$

where ϕ_G, the gas two-phase flow multiplier, depends on a correlation factor that varies with the flow mechanism. Lockhart and Martinelli [21] sought to generalize the correlation factor for the flow multiplier in terms of a new parameter, X, independent of the flow mechanism. Lockhart and Martinelli considered the two fluids separately, formulating the fanning friction factor for each phase, as if each phase occupied a distinct fraction of the cross-sectional area. Under the constraint that the static pressure drop is equal for both phases and the volume occupied by each phase equals the volume of the pipe, the new correlation term becomes:

$$X = \sqrt{\frac{\Delta P_L}{\Delta P_G}} \tag{9}$$

in which ΔP_L and ΔP_G equal the pressure drop experienced along the channel if the respective phase flowed alone in the pipe.

Chisholm [6] recommended a simplified relation between ϕ and X as:

$$\phi_L^2 = 1 + \frac{C}{X} + \frac{1}{X^2} \tag{10}$$

The constant termed Chisholm's parameter, C, takes into account the interaction between the two phases. For air-water flows, Chisholm recommended a value of 5 for the laminar-laminar regime. Eq. (10) holds for the gas as well since:

$$\phi_G^2 = X^2 \phi_L^2 \tag{11}$$

Investigation of mini and microchannels revealed a need for further refinement of the C-value for small scales. Several authors have proposed correlations for the C-value. The correlations fall into two categories, correlations that produce a C-value independent of flow conditions and ones that allow C to vary with test conditions. For a given geometry and fluid pair, Chisholm [6], Mishima and Hibiki [25], Zhang et al. [39], English and Kandlikar [11], and Li and Wu [18] produce a constant C-value regardless of the flow conditions (Table 2). Of the correlations in Table 2, the equations of Zhang et al. [39] and Li and Wu [18] take into account the influence of surface tension (σ) through the confinement number (N_{conf}) defined as:

$$N_{conf} = \sqrt{\frac{\sigma}{g(\rho_L - \rho_G)D_H^2}} \tag{12}$$

and the Bond number (Bo) defined as $1/N_{conf}^2$. The g in Eq. (12) equals the acceleration due to gravity.

Several authors investigated the influence of different dimensionless parameters on the Chisholm parameter (Table 3) that allow C to vary with test conditions. The correlations have several parameters in common. Re_{lo} stands for the liquid-only Reynolds number defined as:

$$Re_{lo} = \frac{GD_H}{\mu_L} \tag{13}$$

and Su_{go} stands for the gas-only Suratman number defined as:

$$Su_{go} = \frac{\rho_G \sigma D_H}{\mu_G^2} \tag{14}$$

For Lee and Lee [17] and Saisorn and Wongwises [29], the dimensionless variables Φ and Λ equate to a capillary number (Ca), and an inverse liquid-only Suratman number, respectively. Li and Hibiki [19] use the two-phase viscosity of McAdams et al. [24] to determine the two-phase viscosity combined with a two-phase density defined as:

$$\rho_{tp} = \chi\rho_G + (1 - \chi)\rho_L \tag{15}$$

to define the two-phase viscosity number as:

$$N_{\mu_{tp}} = \frac{\mu_{tp}}{\left(\rho_{tp}\sigma\sqrt{\frac{\sigma}{g(\rho_L - \rho_G)}}\right)^{0.5}} \tag{16}$$

The correlation of Ma et al. [22] takes into account the channel geometry through the aspect ratio (α) defined as the channel height divided by the channel width.

Table 3
Correlations producing a variable C-value for the separated flow model.

Reference	C correlation	Test conditions
Sun and Mishima [34]	$C = 26\left(1 + \frac{Re_L}{1000}\right)\left[1 - e^{\frac{-0.153}{0.27N_{conf}^2 + 0.8}}\right]$	D_H = 0.506–12 mm
Ma et al. [22]	$C = \hat{a}Ca_L^{\hat{b}}$ $\hat{a} = 7.59 - 0.4237\alpha^{-0.9485} + 0.0023Re_L$ $\hat{b} = 0.223 + 0.2\alpha^{0.9778}$	Channels 100 μm by 200–2000 μm
Kim and Mudawar [16]	$C = 3.5 \times 10^{-5} Re_{lo}^{0.44} Su_{go}^{0.5} \left(\frac{\rho_L}{\rho_G}\right)^{0.48}$	Condensing, Adiabatic flows
Li and Hibiki [19]	$C = 41.7N_{\mu_{tp}}^{0.66} Re_{tp}^{0.42} \chi^{0.21}$	Flow boiling
Lee and Lee [17]	$C = 6.833 \times 10^{-8} \Lambda^{-1.317} \Phi^{0.719} Re_{lo}^{0.557}$	20 mm wide by 0.4–4 mm high Channels
Saisorn and Wongwises [29]	$C = 7.599 \times 10^{-3} \Lambda^{-0.631} \Phi^{0.005} Re_{lo}^{-0.008}$	Round tubes

2.3. Relative permeability models

Another approach to understand the two-phase pressure drop treats the flow as a flow in a porous media. The channel represents a single pore with an absolute permeability of K. Under two-phase flow, the liquid in the channel forms a pore structure that the gas must flow through and vice versa. The presence of the second phase will reduce the available space for the first phase, decreasing the permeability of the first phase. Thus, the effective permeability of a phase should equal K multiplied by a term (the relative permeability, k_r) to account for the influence of the second phase. This allows for a generalization of Darcy's equations for steady-laminar flow in porous media as:

$$\rho_G \vec{U}_G = -\frac{k_{r,G} K}{v_G} \nabla P_G \tag{17}$$

$$\rho_L \vec{U}_L = -\frac{k_{r,L} K}{v_L} \nabla P_L \tag{18}$$

where k_{rG} takes into account the influence of the liquid on the gas and k_{rL} takes into account the influence the gas has on the liquid.

With the goal of understanding the pressure drop between the inlet and outlet of a channel, integrating Eq. (17) between the inlet and outlet with the assumptions that the flow properties change only in the streamwise (z) direction, neglecting surface tension, and accounting for any single phase flow gives [36]:

$$\frac{\Delta P_G}{\frac{\mu_G U_G L}{K}} = \phi_G^2$$

$$\phi_G^2 = \bar{z}^* + \int_{\bar{z}^*}^{1} \frac{1}{k_{r,G}} d\hat{z} \tag{19}$$

where $\bar{z}^*$ equals the location of water injection divided by the length of the channel. The first term in Eq. (19) accounts for any single-phase gas flow at the entrance of the channel and the second term accounts for the interaction of the two phases.

Several authors have modeled the relative gas permeability as a function of liquid saturation (s_L) shown in Table 4. The use of the effective saturation ($s_{L,e}$) takes into account liquid that the gas flow cannot remove from the channel ($s_{L,r}$). In general the relative permeability equations in Table 4 follow a trend of:

$$k_{r,L} = s_{L,e}^{n_k} \tag{20}$$

$$k_{r,G} = (1 - s_{L,e})^{n_k} \tag{21}$$

where n_k represents a generalized exponent. For example, n_k equals 3.05 for the work of Nowamooz et al. [26]. Physically, the n_k represents the degree to which the liquid influences the gas flow—the larger the n_k value, the greater the influence.

The difficulty in experimentally measuring the saturation led other researches to approach the relative permeability model in a different manner. In addition to the relative permeability model in Table 4, Fourar and Bories [12] determined a saturation model. Fourar and Bories [12] measured the liquid saturation in a glass fracture of 1 mm gap spacing and a width of 0.5 m. The small heights compared to the width allowed Fourar and Bories to treat the flow as plane-poiseuille flow and by relating the pressure equation to the Lockhart-Martinelli parameter (X), the authors arrived at

$$s_L = \left(\frac{X}{1+X}\right)^2 \tag{22}$$

Eq. (22) combined with the corresponding relative permeability model (Table 4) showed good agreement with the experimental two-phase pressure for both the glass fracture and baked clay fractures 14 cm wide by 0.54, 0.4, and 0.18 mm high.

Wang [36] arrived at a simplified form for the saturation through the manipulation of Darcy's equations. When neglecting the surface tension, $\nabla P_L = \nabla P_G$ and thus Eqs. (17) and (18) have the gas pressure gradient in common. By combining the two equations through the gas pressure gradient and re-organizing,

$$U_G = \frac{\mu_L}{\mu_G} \frac{k_{r,G}}{k_{r,L}} U_L \tag{23}$$

results for the streamwise direction. Combining Eqs. (20), (21), and (23), gives

$$s_L = \frac{\left(\frac{U_L \mu_L}{U_G \mu_G}\right)^{\frac{1}{n_k}} + s_{L,r}}{\left(\frac{U_L \mu_L}{U_G \mu_G}\right)^{\frac{1}{n_k}} + 1} \tag{24}$$

Thus, the saturation only depends on fluid parameters and the set test conditions for superficial velocities (U). Herein, the two-fluid model refers to the use of Eq. (19) combined with Eqs. (21) and (24). Similar to Chisholm's analysis, the determination of an unknown correlation parameter (n_k) remains.

3. Analytical solution to water film thickness

Steinbrenner [33] noted that in thin microchannels, the stratified flow regime persisted for a wide range of test conditions. The current study predominately generated stratified flow over the range of test conditions, which simplifies the determination of the saturation. Stratified flow forms when a liquid film in contact with a side wall occupies the entire height of the channel but only part of the channel width. Let a equal the channel height, c the film thickness, and $c + b$ the channel width (w). The liquid

Table 4
Relative permeability models.

Reference	$k_{r,G}$ model	Test conditions
X-Model	$k_{r,G} = (1 - s_{L,e})$	
Corey [9]	$k_{r,G} = (1 - s_{L,e})^2 (1 - s_{L,e}^2)$	Oil-gas
Nowamooz et al. [26]	$k_{r,G} = (1 - s_L)^{3.05}$	Air-water, fractures
Chen et al. [4]	$k_{r,G} = 0.502 s_G^3 + 0.1129 s_G^2 + 0.3483 s_G$	Nitrogen-water, fractures
Fourar and Lenormand [13]	$k_{r,G} = (1 - s_L)^3 + \frac{3}{2}\overline{\mu} s_L (1 - s_L)(2 - s_L)$	Air-water, fractures
Huang et al. [14]	$k_{r,G} = (1 - s_L)\left[\frac{3}{2}\overline{\mu} + (1 - s_L)^2 (1 - \frac{3}{2}\overline{\mu})\right]$	LBM Simulation
Fourar and Bories [12]	$k_{r,G} = (1 - \sqrt{s_L})^2$	1.0, 0.54, 0.40, and 0.18 mm Fractures
where	$s_{L,e} = \frac{s_L - s_{L,r}}{1 - s_{L,r}}$	
	$s_G = 1 - s_L$	
	$\overline{\mu} = \mu_G / \mu_L$	

saturation equals the volume of liquid ($a \times c \times L$) divided by the total volume of the channel ($a \times w \times L$), which reduces to the dimensionless water film thickness ratio, $h_{ratio} = c/w$. Thus, determining the liquid saturation requires only measuring the film thickness ratio.

Through a Fourier sine transformation, Tang and Himmelblau [35] determined a series solution to the velocity distribution in each phase under the assumptions of laminar flow with a planar interface (neglect capillary and body forces) and in an infinitely long channel. The boundary conditions impose zero velocity at the walls and equal shear at the interface for both fluids. Steinbrenner [33] reorganized Tang and Himmelblau's equations in terms of dimensionless variables such that the velocity equals a dimensional scaling factor multiplied by a dimensionless function of only $\hat{\mu}, h_{ratio}$, and AR where $\hat{\mu} = \mu_L/\mu_G$ and the aspect ratio (AR) equals w/a. Integrating the velocity in each phase over the cross-sectional area gives the volumetric flow rate of each phase. Taking the ratio of the volumetric flow rates will eliminate the scaling factor, leaving $f(\hat{\mu}, h_{ratio}, AR)$. Setting the fluid pair and the channel geometry fixes AR and $\hat{\mu}$. Therefore the ratio of volumetric flow rates only depends on h_{ratio} (saturation). Experimenters set the volumetric flow rates, fluid pairs, and channel geometry, allowing for the calculation of h_{ratio} for a given experiment without further measurement.

4. Experimental method

The experimental work consists of air-water tests in a rectangular microchannel. The calculation of different parameters rely on standard fluid properties of humid air and water at 20 °C shown in Table 5. Four different liquid flow rates of 177 μL/h, 1.77 mL/h, 59.07 μL/min, and 590.7 μL/min produce superficial liquid velocities of $5.0 \times 10^{-5}, 5.0 \times 10^{-4}, 1.0 \times 10^{-3}$, and 1.0×10^{-2} m/s, respectively. The gas flow rates vary from 30, 50–325 mL/min in 25 mL/min increments producing superficial gas velocities between 0.51 and 5.50 m/s. Characterizing the flow in terms of Reynolds numbers gives a Re_L of 0.0277, 0.277, 0.55, and 5.55 with gas Reynolds numbers varying between 18.2 and 197 for each liquid Reynolds number. The combination of Reynolds numbers produce a liquid-only Reynolds number between 0.35 and 9.19.

Table 5
Fluid properties.

Property	Air	Water
Density (kg/m^3)	1.19	998.3
Viscosity (kg/m·s)	1.846×10^{-5}	1.002×10^{-3}
Surface tension (N/m)	72.86×10^{-3}	

4.1. Experimental assembly

Fig. 1 depicts the testing apparatus for this work, the key component being the microchannel assembly (Fig. 1A) forming a 3.23 mm by 0.304 mm by 164 mm ($w \times h \times L$) rectangular microchannel, aligned horizontally. The geometry results in a hydraulic diameter of 557 μm. Three materials form the walls of the microchannel: 6061 aluminum forming the base, 304 full-hard stainless steel forming the side walls, and polycarbonate forming the top of the channel. The materials exposed to air-water flow result in a hydrophilic microchannel with contact angles of $76° \pm 8°$ for the base, $82° \pm 7°$ for the sides, and $81° \pm 7°$ for the top. In this work, the stated uncertainties are at a 95% confidence level.

Manual milling techniques were used to machine a width of 3.23 mm ±10 μm into the stainless steel. The stainless steel has a manufacture stated thickness tolerance of ±15 μm about the nominal 0.304 mm thickness. The polycarbonate allows optical assess for visualization of the flow. The microchannel assembly builds off the designs of Cho and Wang [7] and Pfund et al. [27] in which layers form the channel. For this apparatus, the seal of the channel comes solely from compression generated by twenty-two bolts torqued to 5.65 N·m (50 in ·lb$_f$).

The formation of the two-phase flow covers several design aspects. Asymmetric water injection occurs 10 mm downstream of the air inlet through a 365 μm hole in the aluminum base (Fig. 2a). Therefore, the first 10 mm of the channel experiences only single-phase air flow. A syringe pump (New Era Pump System NE-300, Fig. 1B) loaded with 1, 10, or 30 mL syringes depending on the flow rate, supplies room temperature (20 °C ± 2 °C) deionized water to the system. MKS100B mass flow controllers inside a Scribner and Associates 850e Fuel-cell Test Station (Fig. 1C) control the air flow from the main air supply within ±20 mL/min. The air passes through a bubble humidifier (Fig. 1D) containing 1500 mL of DI-water to achieve 100% relative humidity before entering the microchannel. A 1 cm hole acts as the inlet manifold while a 1.4 cm hole acts as an outlet manifold. The minimum straight distance between the edge of the manifolds defines the channel length.

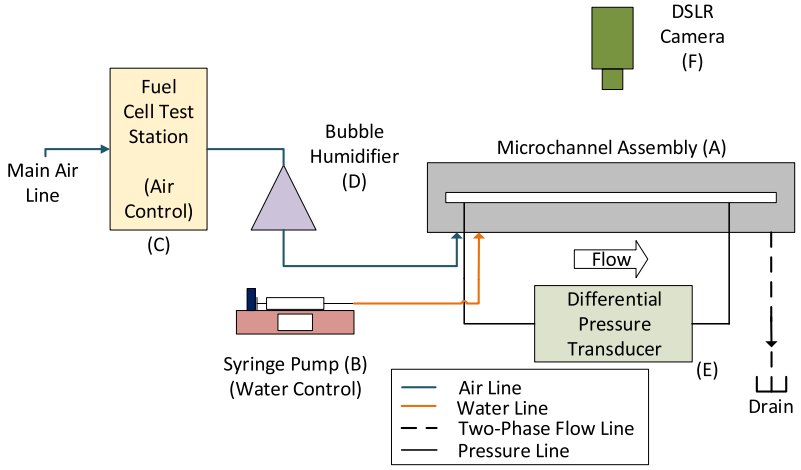

Fig. 1. Schematic diagram of the experimental set-up.

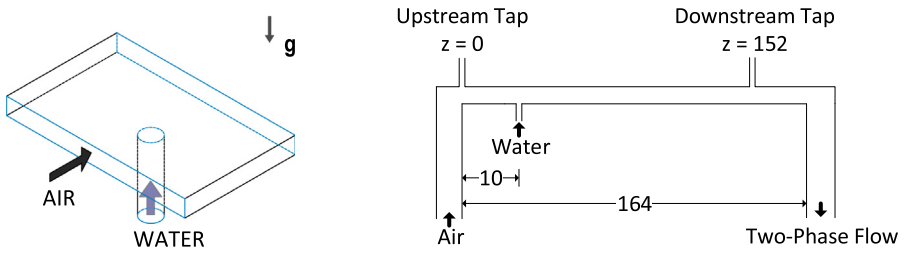

(a) Diagram of asymmetric water injection.

(b) Pressure tap locations. Dimensions are in millimeters.

Fig. 2. Detailed diagram of the microchannel assembly.

4.2. Pressure measurement

The main objective of the work is the measurement of the two-phase pressure drop. A Setra 230 differential pressure transducer (Fig. 1E) with a range of ±0.5 psi (±3.447 kPa) takes the difference between two pressure taps in the microchannel with an accuracy of ±0.0025 psi (±17.2 Pa). The pressure taps align with the channel centerline and consist of 365 μm holes drilled through the optical plate to a depth of 1.27 mm before expanding to a connecting line of 1.58 mm diameter. The design of the taps follows the recommendations of Shaw [32] to minimize static pressure error. The measured pressure difference occurs over a 152 mm length of the channel, with one tap located at the entrance ($z = 0$ mm) and another one located 12 mm before the exit ($z = 152$ mm) as shown in Fig. 2b.

4.3. Data acquisition

The Setra 230 has a manufacturer stated response time of 2 ms. This corresponds to 500 Hz. A digital filter (Alligator USBPGF-S1) filters the pressure transducer's output at 700 Hz before a data acquisition card (DATAQ DI-245) logs the signal at 2000 samples per second. To maximize the dynamic range of the data acquisition card, a precision buck and gain amplifier subtracts out the mean voltage before amplifying the signal by a factor of 100.

4.4. Visualization and saturation measurements

In this work, the flow forms as a stratified flow and the visualization of the flow formation will allow for the determination of the liquid saturation. Several techniques exist to visualize the flow: laser-induced fluorescence [33], Schlieren [5], and shadowography based on back-lighting. This work applies a simplified approach relying on the shadow generated by the interface of the two phases. Unlike shadowography, this method does not utilize back-lighting, allowing for the use of any base material for the channel. The clear polycarbonate sheet forming the top of the channel gives optical access for a DSLR camera (Canon Rebel T3) to capture images of the entire channel length in 5 s intervals (Fig. 1F). Fig. 3a shows an actual image of the stratified flow that occurs in this work and Fig. 3b shows the extracted film in physical units. Note that both images have a compressed aspect ratio leading to the waviness of the film and that the inversion of Fig. 3a occurs due to how MATLAB assigns pixel indices. Extracting the saturation from the images is done through image processing in MATLAB. The application of a Laplacian of the Gaussian filter shows the location of intensity gradients—specifically the intensity gradient at the air-water interface. A Wiener filter removes noise. Plotting the contour matrix of the image allows for the determination of the intensity corresponding to the air-water interface. Extracting the corresponding pixel numbers and converting to a physical unit system gives the film thickness.

The film thickness, shown in Fig. 3b where the water lies between the x-axis and the black line, varies over the length of the channel. Therefore, for comparison to Steinbrenner [33] and for use in the relative gas permeability models, an equivalent film thickness is defined. Trapezoidal numerical integration of the film thickness data gives the area of water in the channel. Dividing the area of water by the length of the film gives an equivalent film thickness—essentially a film that has the same area as the experimental measurement but produces a flat interface between the fluids. Eighty pixels compose the width of the channel (3.23 mm), meaning each pixel represents 0.04 mm. The Wiener filter smooths the data over two pixels and the location of the wall can fall within two pixels as well. The film thickness ratio (h_{ratio}) equals the location of the film minus the location of the wall, all divided by the channel width. Through the Kline-McClintock method, the uncertainty of the film thickness equals 0.11 mm or equivalently 0.035

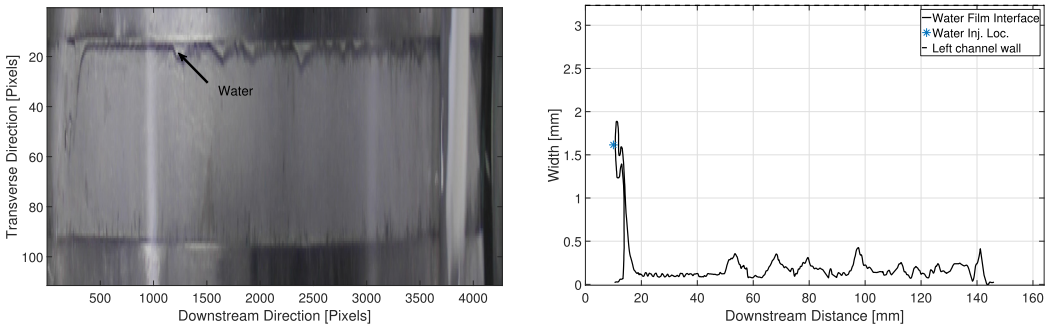

(a) Cropped image of the channel.

(b) Extracted Water film.

Fig. 3. Water film for experimental conditions of $U_L = 1.0 \times 10^{-3}$ m/s and $U_G = 3.81$ m/s (flow from left to right).

for the h_{ratio}. The propagation of the error through the numerical integration to define the equivalent film thickness gives the same uncertainty, neglecting the uncertainty of the length.

5. Results and discussion

5.1. Single-phase validation

The variability in two-phase pressure models shown in Section 2 prevents validation of the experimental set-up with two-phase flow. Therefore, single-phase gas flow experiments were conducted for validation. For single phase flow, Eq. (2) still holds with G replaced by $\rho_G U_G$ and ρ_{tp} replaced by ρ_G. Eq. (4) still defines the friction factor with Re_{tp} replaced by Re_G. For single-phase flow in a rectangular duct, the Darcy friction factor depends on the aspect ratio of the channel as:

$$\overline{C} = 96(1 - 1.35532\alpha^* + 1.9467\alpha^{*2} - 1.7012\alpha^{*3} + 0.9564\alpha^{*4} - 0.2537\alpha^{*5}) \quad (25)$$

given by Kakac et al. [15] from fitting the exact solutions of Shah and London [31] for different aspect ratios (α^*). In this case, the aspect ratio (α^*) equals the smallest dimension divided by the largest dimension. Fig. 4 shows the comparison between the experimentally measured pressure drop and the theoretical value. The data fall within ±4% for all experiments except for the two lowest. At 0.51 m/s and 0.85 m/s, the measurements fall below the theoretical value by 17% and 7%, respectively. The error bars for pressure in Fig. 4 account for the ±17.2 Pa accuracy of the pressure transducer. The superficial gas velocity equals the volumetric flow rate of gas divided by the cross-sectional area. Utilizing the Kline-McClintock method for the equation $U_G = Q_G/A_c$, gives a velocity uncertainty of ±0.34 m/s at $U_G = 0.51$ m/s to ±0.43 m/s at $U_G = 5.5$ m/s.

The location of the first tap ($z = 0$) means that pressure measurements will include entrance effects. To account for the entrance effects, Shah defines an apparent Fanning friction factor [30] to replace Eq. (4). Comparing the experimental data to the correlation proposed by Shah [30], the data fall within ±3% for all experiments except the two lowest that show negligible change (Fig. 4). Therefore, the inclusion of the entrance region has minimal influence on the measured pressure drop.

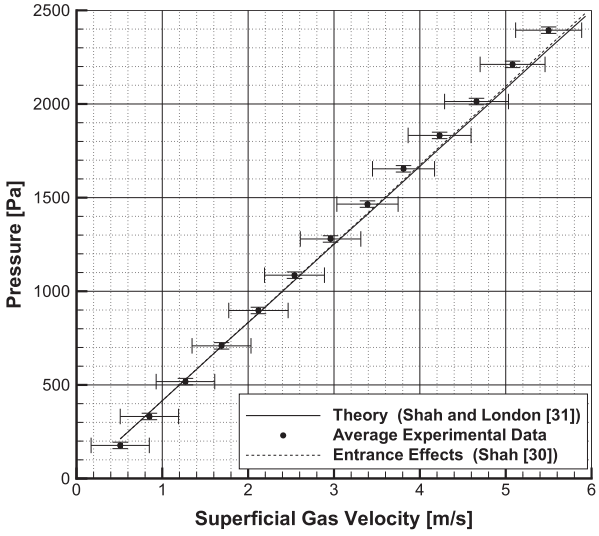

Fig. 4. Comparison of theoretical and experimental single-phase gas pressure drop versus superficial gas velocity.

5.2. Two-phase pressure results

Characterizing the two-phase pressure drop relies on the gas two-phase flow multiplier (ϕ_G^2). Experimentally determining ϕ_G^2 consists of measuring the single-phase pressure drop for gas flow and then measuring the two-phase pressure drop after water injection begins—the two-phase pressure drop divided by the single-phase gas pressure drop determines ϕ_G^2. Fig. 5 shows ϕ_G^2 versus superficial gas velocity for the four different liquid velocities. Each experimental datum represents a 30 min average (5 min for the highest U_L) of the measured two-phase pressure, while the average data represent the average of all the experimental data for a given case. The application of the Kline-McClintock method on the equation $\phi_G^2 = \Delta P_{tp}/\Delta P_G$ determines the magnitude of the error bars. As the superficial gas velocity increases, the gas two-phase flow multiplier decreases. Increasing the superficial liquid velocity results in an increase in ϕ_G^2. During the experiments for $U_L = 1 \times 10^{-2}$ m/s for $U_G = 0.51$–1.27 m/s the flow behaved plug-like causing water to enter the pressure taps. As a result, the analysis did not include data in that range. Of particular note, the majority of the data falls within the measurement uncertainty. Several points however, fall outside the uncertainty range. Under the same experimental conditions, the stratified flow showed differences in film thickness between experiments and thus produced differences in the measured pressure. Additionally, Fig. 5a and b at $U_G = 0.51$ and 5.08 m/s show ϕ_G^2 dropping below 1. These measurements do not make physical sense and the uncertainty in the measurement accounts for this behavior.

5.3. Comparison of the experimental data to existing two-phase pressure models

Section 2 presented three approaches to predicting the two-phase pressure drop accompanied by several different correlations derived for a variety of conditions. This section will look at how the experimental data compares to the existing models to reveal which models best predict the experimental data.

5.3.1. Statistical method for model comparison

Determining how well models predict the experimental data relies on statistics of the error. As defined by Li and Hibiki [19], the error (δP_i) equals the two-phase pressure drop calculated from the model ($\Delta P_{pre,i}$) minus the experimentally measured pressure drop ($\Delta P_{exp,i}$) for the *ith* experimental datum. Defining the percent error ($\delta^* P_i$) as the error (δP_i) divided by $\Delta P_{exp,i}$ gives a scale independent comparison. The mean absolute percent error defined as:

$$|\bar{e}_{\%}| = \frac{1}{n}\sum_{i=1}^{n}|\delta^* P_i| \quad (26)$$

serves as the primary basis of comparison in this work and the cited works. The mean absolute error prevents individual errors from canceling out and thus gives the best indication of the error. Researchers typically quantify the percentage of data points that fall within a given range [18,34,16,17]. Defining the root-mean-square percent error ($\sigma_{\%}$) as:

$$\sigma_{\%} = \left(\frac{1}{n}\sum_{i=1}^{n}(\delta^* P_i)^2\right)^{0.5} \quad (27)$$

will indicate the range of the data. For example, a $\sigma_{\%} = 15\%$ indicates 68% of the data fall within ±15% or 95% of the data fall within ±30%, for normally distributed errors. While Eqs. (26) and (27) represent scale independent quantities, scale dependent quantities provide further insight. The mean error ($\bar{e}$) defined as:

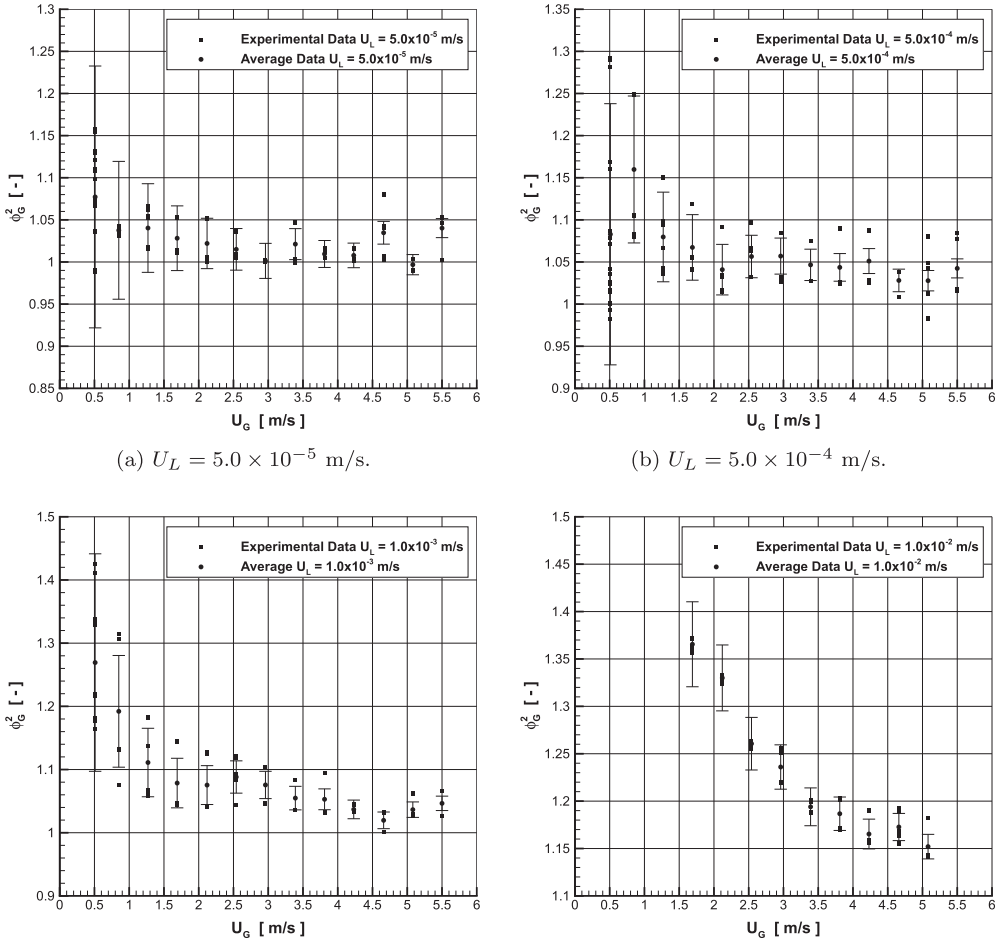

(a) $U_L = 5.0 \times 10^{-5}$ m/s. (b) $U_L = 5.0 \times 10^{-4}$ m/s.

(c) $U_L = 1.0 \times 10^{-3}$ m/s. (d) $U_L = 1.0 \times 10^{-2}$ m/s.

Fig. 5. Experimental gas two-phase flow multiplier versus superficial gas velocity.

$$\overline{e} = \frac{1}{n}\sum_{i=1}^{n} \delta P_i \tag{28}$$

where n equals the number of data points, demonstrates the trend in the data. A positive mean error shows the model over-predicts the experimental data, while a negative mean error shows an under-prediction. Taking the mean percent error ($\overline{e}_{\%}$) defined as:

$$\overline{e}_{\%} = \frac{1}{n}\sum_{i=1}^{n} \delta^* P_i \tag{29}$$

represents the mean error independent of the scale. Finally, utilizing the root-mean-square error (σ_e) defined as:

$$\sigma_e = \left(\frac{1}{n}\sum_{i=1}^{n} (\delta P_i)^2\right)^{0.5} \tag{30}$$

indicates the variation of the error, which helps to determine how well the models collapse the experimental data to the prediction. Eqs. (26)–(30) will serve as the basis of comparison between different the selected prediction to understand the differences between models.

Figures plotting the experimentally measured two-phase pressure (ΔP_{exp}) versus the value predicted by the two-phase pressure models (ΔP_{pre}) help reinforce the statistics. The solid line in Figs. 6–10 represent a one to one prediction—i.e. the model perfectly predicts the two-phase pressure measurements. Each figure also shows the individual data points for the four superficial liquid velocities. Data above the solid line indicates the model under-predicts the experimental data whereas data below the solid line indicates an over-prediction.

5.3.2. Homogeneous flow model comparison

Table 6 summarizes the overall error statistics for the homogeneous flow models for all of the data. The models compared poorly to the experimental data by every metric, except for the viscosity models of Dukler et al. [10] and Beattie and Whalley [3]. The model of Dukler et al. under-predicted the two-phase pressure drop (Fig. 6a) with the smallest $\overline{e} = -32$ Pa at $U_L = 5.0 \times 10^{-5}$ m/s and increasing to $\overline{e} = -102$ Pa at $U_L = 1.0 \times 10^{-2}$ m/s. Thus, the predictive accuracy for the model of Dukler et al. decreases as the superficial liquid velocity increases for this experiment even though the mean absolute percent error equals 6.6%. Beattie and Whalley's model initially outperforms Dukler et al. having a $\overline{e} = -30$ Pa at $U_L = 5.0 \times 10^{-5}$ m/s to $\overline{e} = -11$ Pa at $U_L = 1.0 \times 10^{-3}$ m/s with a smaller scatter in this range (a σ_e of 64 Pa versus 77 Pa on average). At $U_L = 1.0 \times 10^{-2}$ m/s, Beattie and Whalley's model over-predicts the two-phase pressure (Fig. 6b) with a $\overline{e} = 420$ Pa ($|\overline{e}_{\%}| = 30\%$), leading to the overall root-mean-square error of 230 Pa. Based on the analysis, the viscosity model of Dukler et al. produces too low of a two-phase viscosity while Beattie and Whalley's two-phase viscosity increases too rapidly at higher liquid superficial velocities for this experiment.

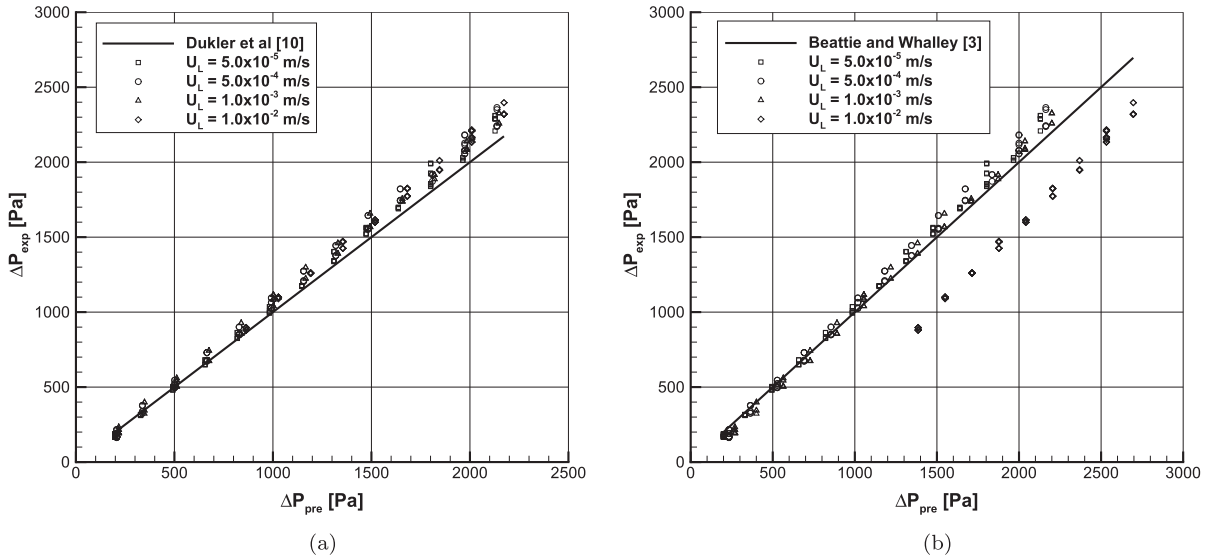

Fig. 6. Comparison between experimental and predicted two-phase pressure drop for homogeneous flow models.

5.3.3. Separated flow model comparison

Of the correlations that produce a constant *C*-value for a given fluid pair and geometry, the correlation of English and Kandlikar [11] predicted the data the best (Table 7). The model of English and Kandlikar over-predicted the two-phase pressure with the mean error increasing from a $\bar{e} = 2.09$ Pa at $U_L = 5.0 \times 10^{-5}$ m/s to $\bar{e} = 364$ Pa at $U_L = 1.0 \times 10^{-2}$ m/s (Fig. 7d). The other correlations shown in Table 7 also over-predict the two-phase pressure for all superficial liquid velocities with the error increasing as the superficial liquid velocity increases (Fig. 7). Statistically speaking, the homogeneous flow model of Dukler et al. [10] out performed the separated flow model of English and Kandlikar [11] for this experiment as the model of English and Kandlikar did not collapse the data over the range of test conditions ($\sigma_e = 202$ Pa).

By allowing the *C*-value to vary with flow conditions, the correlations statistically performed far better than the homogeneous model or correlations with constant *C*-values (Table 8). Lee and Lee [17] derived their model accounting for a slug velocity. Since the flow in this work formed as a stratified flow, the slug velocity does not apply and instead was replaced by the superficial gas velocity. Saisorn and Wongwises [29] replaced the slug velocity with the total superficial velocity. For this experiment, using the total superficial velocity negligibly changed the *C*-value, due to the low superficial liquid velocities. The correlations of Kim and Mudawar[16] and Lee and Lee [17] behave nearly identically (Table 8), deviating at $U_L = 1.0 \times 10^{-2}$ m/s with $\bar{e} = -57$ Pa and $\bar{e} = -50$ Pa, respectively. Visually the difference becomes indistinguishable (Fig. 8d and e). Although undiscernible in the figures, the models show an increasing mean error as the superficial velocity increases with $\bar{e} = -22$ Pa to $\bar{e} = -44$ Pa from $U_L = 5.0 \times 10^{-5}$ m/s to $U_L = 1.0 \times 10^{-3}$ m/s. Although not originally intended for thin microchannels, the analysis shows the correlations of Kim and Mudawar [16] and Lee and Lee [17] reasonably predict the experimental data.

The correlations of Ma et al. [22] and Li and Hibiki [19] also well predict the experimental data. Unlike Lee and Lee and Kim and Mudawar, Ma et al. [22] initially under-predicts the data ($\bar{e} = -19$ Pa to -15 Pa) before over-predicting the data at $U_L = 1.0 \times 10^{-2}$ m/s with $\bar{e} = 136$ Pa (Fig. 8b). This explains the low mean percent error ($\bar{e}_{\%} = 0.9\%$) but a large mean absolute percent error ($|\bar{e}_{\%}| = 5.0\%$). Li and Hibiki [19] generally over-predicts the data. Initially, the correlation only differs by $\bar{e} = 10$ Pa at the lowest U_L but increases to $\bar{e} = 219$ Pa at $U_L = 1 \times 10^{-2}$ m/s. The variation with U_L leads to a σ_e of 125.5 Pa, with the data at $U_L = 1.0 \times 10^{-2}$ m/s consistently different than the prediction (Fig. 8c).

The work of Li and Hibiki [19] requires further discussion. Fig. 5 shows that the gas two-phase flow multiplier decreases with increasing superficial gas velocity. The correlation of Li and Hibiki [19] produces varying trends for ϕ_G^2 depending on the superficial liquid velocity. For $U_L = 1.0 \times 10^{-3}$ and 1.0×10^{-2} m/s, the trend of ϕ_G^2 agrees with the experimental trend. However, the correlation results in an increasing ϕ_G^2 with increasing U_G at $U_L = 5.0 \times 10^{-5}$ m/s. Conversely, at $U_L = 5.0 \times 10^{-4}$ m/s, the correlation predicts ϕ_G^2 decreasing until $U_G = 3.81$ m/s and increasing thereafter. Li and Hibiki [19] arrived at the correlation for flow boiling. Kim and Mudawar [16] noted that boiling flows behave differently than condensing and adiabatic flows, meaning flow boiling should have its own specific correlations. Even though the model of Li and Hibiki [19] reasonably predicted the two-phase pressure, the trend did not align with the experimentally observed behavior likely due to the correlation being based on experimental data for flow boiling.

5.3.4. Relative permeability model comparison

Using Eq. (19) with the X-Model outperformed the other relative permeability models based on the experimentally measured saturation (Table 9). The X-Model over-predicted the two-phase pressure drop (Fig. 9f) for the three lowest liquid superficial velocities with a mean error of 6.4, 10.9, and 9.23 Pa, respectively. At $U_L = 1.0 \times 10^{-2}$ m/s, the X-model under-predicts the data by 26.9 Pa. The model proposed by Corey [9] performs the second best of the relative permeability models. However, the model of Corey [9] shows an increasing trend in over-predicting the data ($\bar{e} = 38.5$–338.7 Pa) with increasing superficial liquid velocity (Fig. 9a). The other models also over-predict the two-phase pressure drop and show σ_e increasing as the superficial liquid velocity increases (Fig. 9), including the model of Fourar and Bories [12] using the accompanying saturation model (Eq. (22)). Additionally, the models of Fourar and Lenormand [13] and Huang et al. [14] behave identically due to small viscosity ratio (Table 9).

Physically, the relative permeability exponent of 1 for the X-Model means the two fluids minimally impede one another [4].

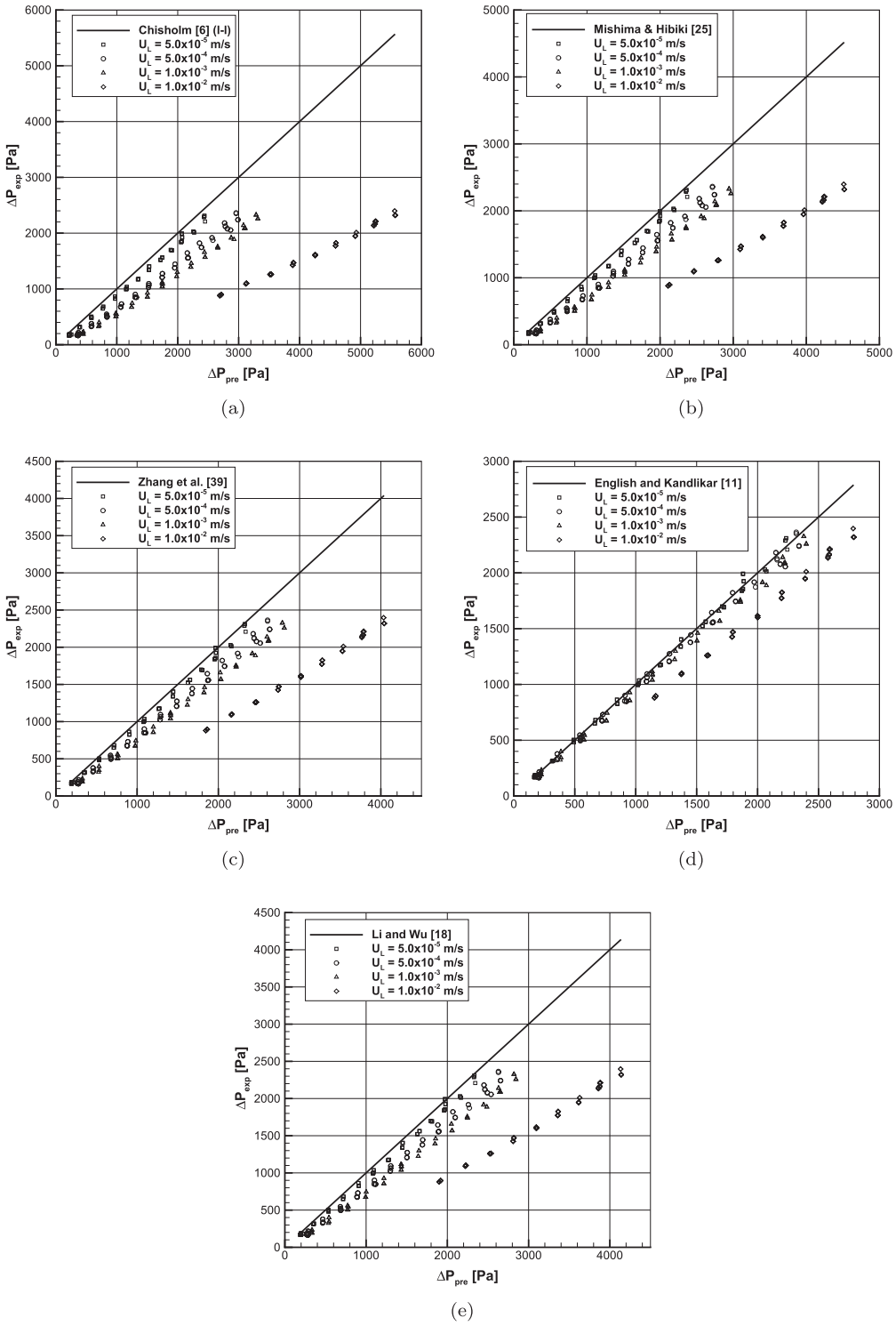

Fig. 7. Comparison between experimental and predicted two-phase pressure drop for Chisholm correlations producing a constant *C*-value.

In stratified flow the gas essentially flows along a channel equal to the channel width minus the water film thickness; the water flows in a channel equal to the water film thickness. Thus, the fluids only interact at the air-water interface. The other relative permeability models with an exponent greater than 1 thus over-predict the interaction of the phases resulting in the over-prediction of the two-phase pressure drop. Since the X-model slightly under-predicts the experimental data while the model of Corey [9] over-predicts the data, the n_k value for the two-fluid model should fall between a value of 1 used by the X-Model and 2 used to leading order by the model of Corey [9].

5.4. Determination of n_k for stratified flow

The previous section detailed a comparison between existing models and the experimental data. The *C*-value correlations of Kim and Mudawar [16] and Lee and Lee [17] predicted the experimental data the best out of the homogeneous and separated flow models

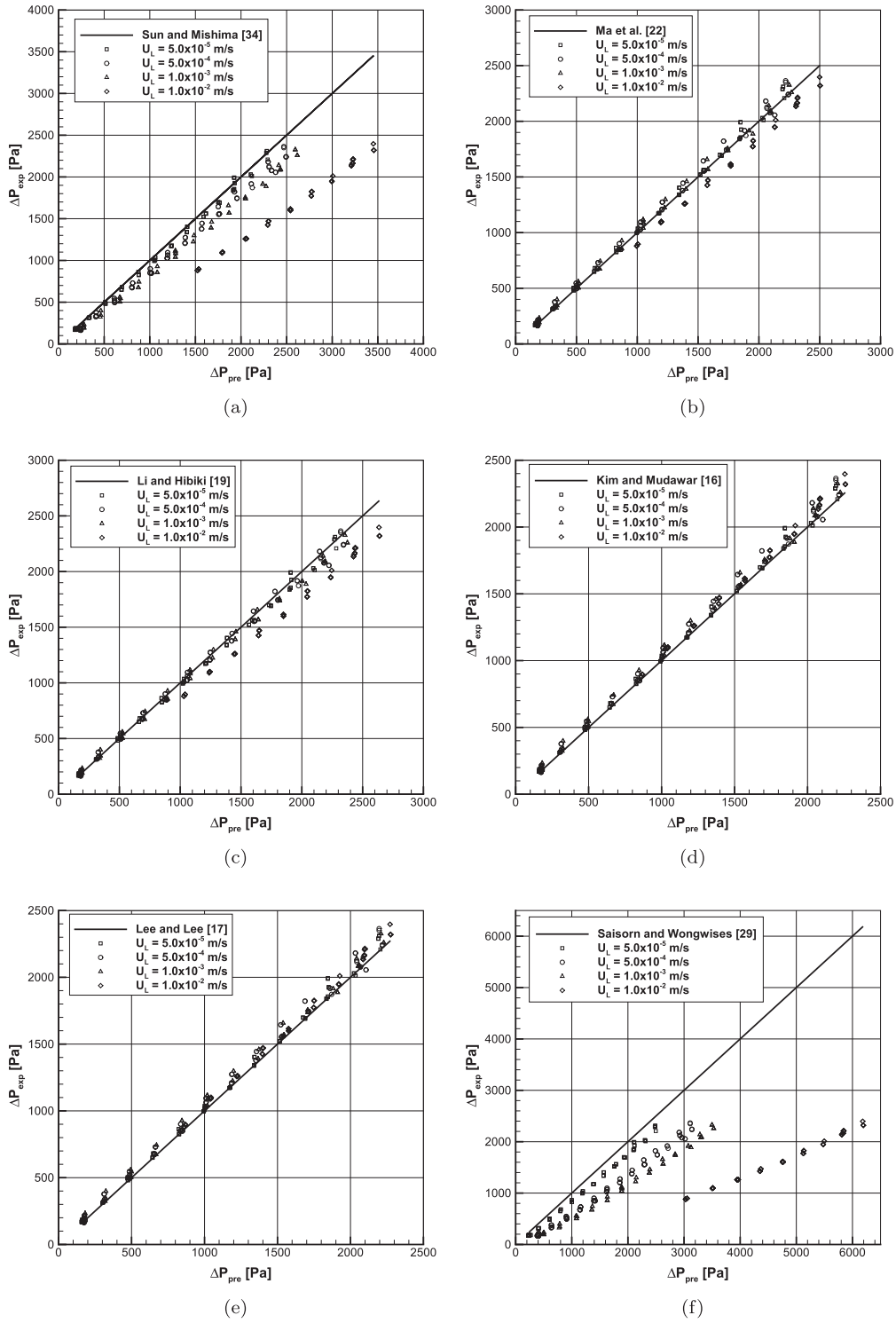

Fig. 8. Comparison between experimental and predicted two-phase pressure drop for Chisholm correlations that vary based on flow conditions.

with a mean absolute percent error of 4.2% and 4.1%, respectively. Overall, the X-Model produced the lowest mean absolute percent error (3.32%) of the compared models. A new model cannot improve the result too much and will only prove beneficial if the model reduces the complexity of determining the two-phase pressure drop. Looking at the *C*-value equations of Lee and Lee [17] and Kim and Mudawar [16], one could optimize the equation by modifying the leading constant or one of the three exponents. The two-fluid model on the other hand only requires a single correlation parameter. Although straightforward to use, the X-model relies on experimentally measured saturation, which proves difficult to measure. As the two-fluid model depends only on a single correlation constant and models the saturation, the two-fluid model simplifies the prediction of the two-phase pressure drop.

5.4.1. Determining n_k from two-phase pressure

Cho and Wang [7] previously determined n_k values for slug, wavy, and annulus flow patterns in a regular fuel cell channel.

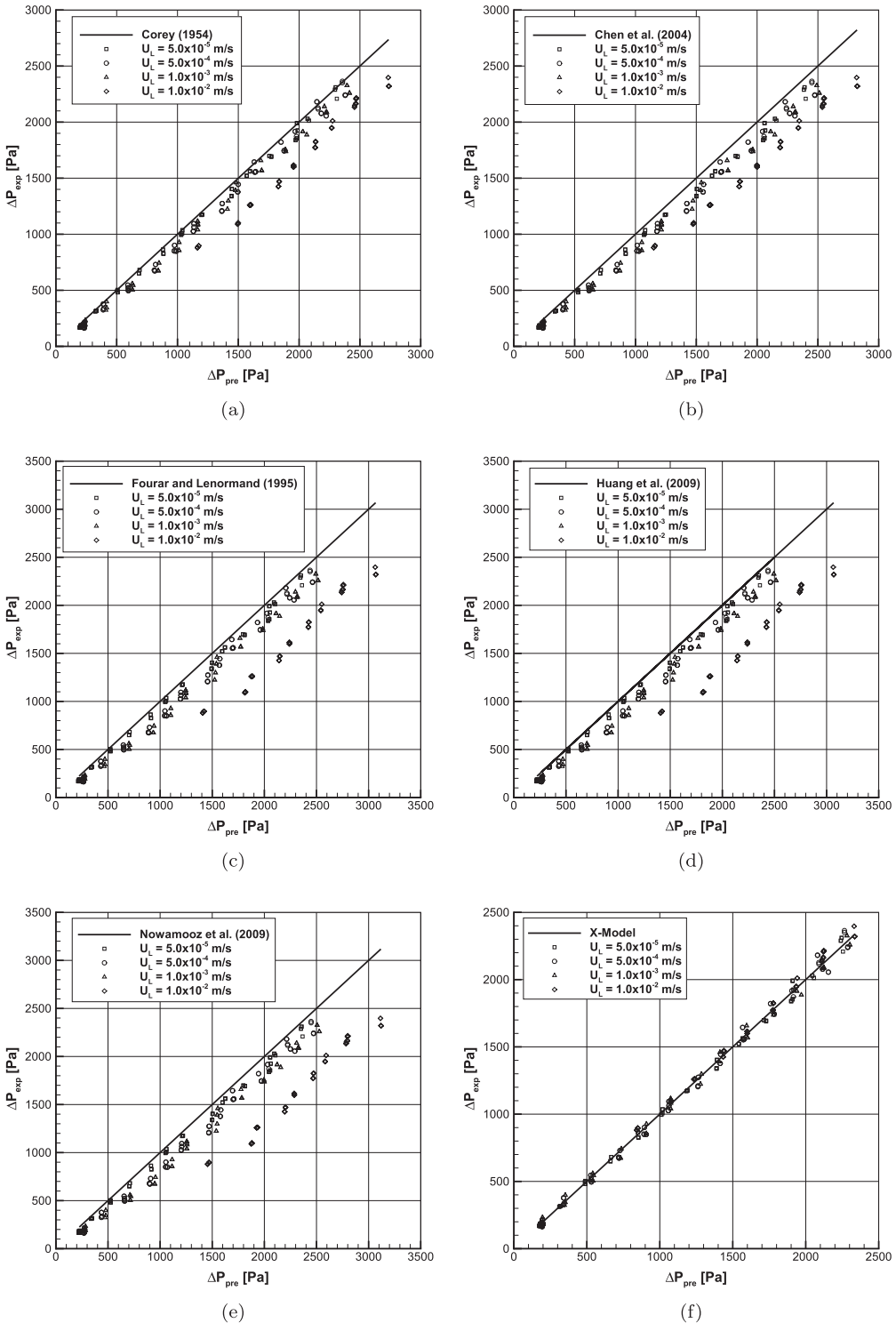

Fig. 9. Comparison between experimental and predicted two-phase pressure drop for relative permeability models using experimentally measured saturation.

The determination of an n_k value for stratified flow follows. In the experiments water did not remain in the channel after water injection stopped; thus, the residual water ($s_{L,r}$) equals zero. This simplifies Eq. (24) and reduces the effective saturation to the liquid saturation. This leaves only the determination of the correlation constant, n_k.

Optimizing the entire data set to minimize the variance between the experimental data and the prediction led to an n_k value of 1.159. Table 10 shows the error statistics for the optimization. The n_k value resulted in an under-prediction of the two-phase pressure by a mean error of −11.91 Pa and produces a mean absolute percent error of 3.25%. Since the optimization minimizes the variance, the standard deviation of the error represents the smallest possible value for this optimization and thus well collapses the data (Fig. 10). Tables 11 and 12 show the error statistics for each superficial liquid velocity correlated by $n_k = 1.159$. Based on the

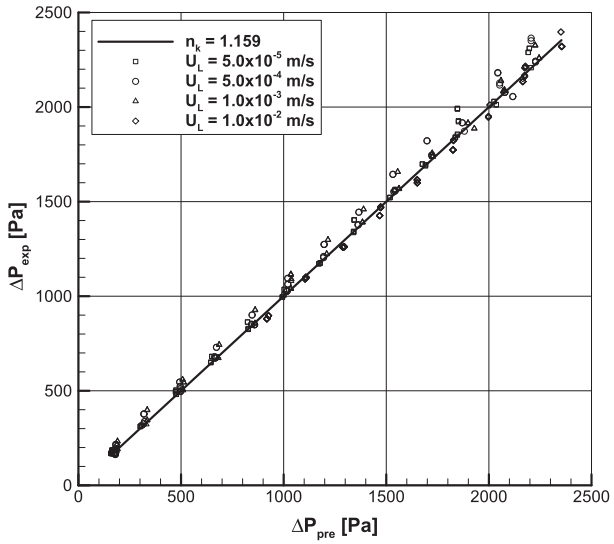

Fig. 10. Comparison between experimental and predicted two-phase pressure drop for the optimized n_k value in Eq. (24).

mean absolute percent error, the selection of the $n_k = 1.159$ agrees best at the lowest and highest superficial liquid velocity. The optimized n_k value under-predicts the majority of the data, except over-predicts the data at $U_L = 1.0 \times 10^{-2}$ m/s with a mean error of 21.92 Pa.

The change from under-predicting to over-predicting suggests the n_k value could vary with test parameters. To understand the variation requires investigating the optimization of the n_k value for each superficial velocity data set. Tables 11 and 12 show the error statistics of the optimized n_k value for each data set compared to $n_k = 1.159$. The comparison to $n_k = 1.159$ shows the opposite trend in the mean error, in which the model over-predicts the data but at $U_L = 1.0 \times 10^{-2}$ m/s the model under-predicts the data. Comparison of the other error statistics show a modest improvement.

The optimization at $U_L = 5.0 \times 10^{-4}$ m/s stands as an outlier. Optimization about the mean ϕ_G^2 for each superficial gas velocity, instead of the individual data points, did not change the n_k value. Conversely, by removing the data for $U_G = 0.51$ to 1.27 m/s, the n_k value changed by $-0.065, 0.135$, and -0.037, for the U_L between 5.0×10^{-5} and 1.0×10^{-3} m/s, respectively. The uncertainty at low superficial gas velocity at $U_L = 5.0 \times 10^{-4}$ m/s, particularly $U_G = 0.51$ m/s that shows several points at the low end of the uncertainty (Fig. 5b), causes the n_k value to not follow the overall trend of n_k decreasing with increasing U_L. For $U_L = 5.0 \times 10^{-4}$ m/s, the n_k equals 1.436 when neglecting the data at $U_G = 0.51$ m/s.

Additionally, the theoretical velocity profiles determined by Tang and Himmelblau [35] and analyzed by Steinbrenner [33] provide further insight (Section 3). Steinbrenner showed that the thick water films have a parabolic profile characteristic of pressure driven flows whereas thin water films have a linear profile characteristic to a shear driven flow. Therefore, the influence of water on the air changes, which could account for the variation of n_k between the data sets (Tables 11 and 12) and the prediction trend of the X-model. Nonetheless, attempts to correlate the change in n_k with dimensionless parameters showed no clear correlation. Therefore, the n_k value should equal 1.159 for stratified flow and remain constant. The universality of $n_k = 1.159$ can only be known as researchers add experimental work for various geometries and fluid pairs that produce stratified flow.

5.4.2. Comparison of determined n_k to measured water film thickness

The saturation model defined in Eq. (24) has not previously been validated against saturation measurements. Fig. 11 compares the experimental saturation and the saturation calculated using Eq. (24) with $n_k = 1.159$. The behavior of the saturation follows the mean error trend of the two-phase pressure shown in Tables 11 and 12. From $U_L = 5.0 \times 10^{-5}$ m/s to $U_L = 1.0 \times 10^{-3}$ m/s, Eq. (24) initially under-predicts the saturation but over-predicts the saturation at $U_L = 1.0 \times 10^{-2}$ m/s. This trend explains the differences between the optimized n_k value and the X-model. To account for the under-prediction of the experimentally measured saturation used in the X-model, the two-fluid model would have to predict a greater interaction of the fluids to compensate for the difference. Conversely, the experimental method over approximates the thickness of the film due to the inability to account for the curvature of the interface, which would allow the X-model to have a lower relative permeability exponent than the two-fluid model. Overall, the predicted saturation of the two-fluid model produces a mean error of -0.035 with a root-mean-square error of 0.045 compared to the experimental data.

Fig. 11 also shows the comparison between the experimental data, the analytical solution presented by Steinbrenner [33], and the saturation model of Fourar and Bories [12]. The experimental data follow the same trend as the analytical solution, the h_{ratio} decreases with increasing ratio of volumetric flow rates. Additionally, the data consistently fall above the analytical solution, as expected due to the inability to account for the curvature of the interface. Steinbrenner [33] showed similar characteristics when comparing experimental measurements to the analytical solution. The two-fluid model produces a higher saturation at low volumetric flow rate ratios and a lower saturation at higher volumetric flow rate ratios compared to Steinbrenner [33] but follows the overall trend. The saturation model of Fourar and Bories [12] defined by Eq. (22) under-predicts the experimental data, the analytical solution, and the two-fluid model. Fourar and Bories [12] derived Eq. (22) based on plane-poiseuille flow, which does not well represent stratified flow when the flow forms between the narrow height of the channel instead of across the channel width. Based on the analysis, the two-fluid model correlates well with the experimental data for both saturation and two-phase pressure.

Table 6
Overall error statistics of the homogeneous flow models.

	$\bar{e}$ (Pa)	σ_e (Pa)	$\bar{e}_{\%}$	$\sigma_{\%}$	$\lvert\bar{e}_{\%}\rvert$
Dukler et al. [10]	−62.7	89.07	−2.2%	8.2%	6.6%
Beattie and Whalley [3]	102.2	230	11.1%	20.5%	14.3%
Fourar and Bories [12]	350	512	32.6%	42%	33%
McAdams et al. [24]	834	1447	70%	110%	71%
Lin et al. [20]	1616	2824	133%	217%	134%
Awad and Muzychka [2]	2445	4117	201%	305%	202%
Cicchitti et al. [8]	18016	27044	1531%	1956%	1531%

Table 7
Overall error statistics of separated flow models using correlations producing constant C values.

	$\overline{e}$ (Pa)	σ_e (Pa)	$\overline{e}_{\%}$	$\sigma_{\%}$	$\lvert\overline{e}_{\%}\rvert$
English and Kandlikar [11]	127.6	201.7	9.8%	14.2%	10.6%
Zhang et al. [39]	522.6	758.2	42.0%	53.1%	42.0%
Li and Wu [18]	553.7	802.1	44.5%	56.1%	44.6%
Mishima and Hibiki [25]	673.5	971.6	54.3%	68.1%	54.3%
Chisholm [6]	1005	1440	81.3%	101%	81.3%

Table 8
Overall error statistics of separated flow models using correlations producing variable C values.

	$\overline{e}$ (Pa)	σ_e (Pa)	$\overline{e}_{\%}$	$\sigma_{\%}$	$\lvert\overline{e}_{\%}\rvert$
Kim and Mudawar [16]	−40.1	55.0	−3.9%	5.6%	4.2%
Lee and Lee [17]	−37.7	52.3	−3.8%	5.6%	4.1%
Ma et al. [22]	25.1	81.31	0.9%	6.5%	5.0%
Li and Hibiki [19]	73.4	125.5	4.2%	8.5%	6.7%
Sun and Mishima [34]	337.4	497.1	26.9%	34.7%	27.0%
Saisorn and Wongwises [29]	1203.5	1718.6	97.6%	120.8%	97.6%

Table 9
Overall error statistics of the relative permeability models.

	$\overline{e}$ (Pa)	σ_e (Pa)	$\overline{e}_{\%}$	$\sigma_{\%}$	$\lvert\overline{e}_{\%}\rvert$
X-Model	−1.1	36.2	0.64%	4.79%	3.32%
Corey [9]	145.8	195.1	14.2%	17.8%	14.3%
Chen et al. [4]	187.5	229.6	17.6%	20.2%	17.6%
Fourar and Lenormand [13]	266.2	356.3	25.3%	31.0%	25.3%
Huang et al. [14]	266.2	356.3	25.3%	31.0%	25.3%
Nowamooz et al. [26]	285.1	383.0	27.1%	33.2%	27.1%
Fourar and Bories [12]	344.3	505.1	27.5%	35.3%	27.6%

Table 10
Overall error statistics for the optimized n_k value.

	$\overline{e}$ (Pa)	σ_e (Pa)	$\overline{e}_{\%}$	$\sigma_{\%}$	$\lvert\overline{e}_{\%}\rvert$
$n_k = 1.159$ (Current study)	−11.91	41.63	−1.58%	4.72%	3.25%

Table 11
Comparison between different n_k values for the two lowest U_L.

	$U_L = 5.0 \times 10^{-5}$ m/s		$U_L = 5.0 \times 10^{-4}$ m/s	
n_k	1.159	1.675	1.159	1.271
$\overline{e}$ (Pa)	−20.31	0.95	−26.49	−15.98
σ_e (Pa)	39.34	32.08	49.11	43.15
$\overline{e}_{\%}$	−2.84%	0.20%	−2.22%	−0.61%
$\sigma_{\%}$	4.29%	2.85%	5.91%	5.87%
$\lvert\overline{e}_{\%}\rvert$	3.02%	2.31%	4.39%	4.20%

Table 12
Comparison between different n_k values for the two highest U_L.

	$U_L = 1.0 \times 10^{-3}$ m/s		$U_L = 1.0 \times 10^{-2}$ m/s	
n_k	1.159	1.363	1.159	1.120
$\overline{e}$ (Pa)	−28.45	7.35	21.92	−4.77
σ_e (Pa)	44.28	34.96	32.87	26.07
$\overline{e}_{\%}$	−3.48%	0.55%	1.61%	−0.12%
$\sigma_{\%}$	5.77%	4.35%	2.24%	1.42%
$\lvert\overline{e}_{\%}\rvert$	3.85%	3.63%	1.91%	1.20%

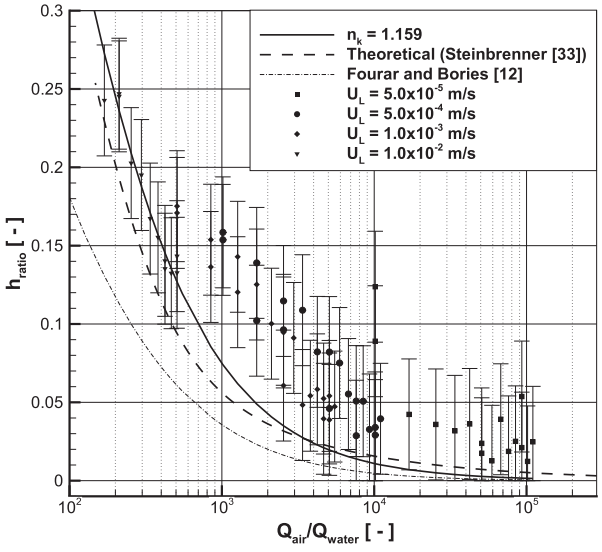

Fig. 11. Comparison between the experimental dimensionless water film thickness, the model of Fourar and Bories [12], the analytical solution of Steinbrenner [33], and the optimized n_k value.

6. Conclusion

This work conducted an experimental study of air-water two-phase frictional pressure drop in a microchannel of dimensions 3.23 mm wide by 0.304 mm high by 164 mm long. The test conditions produced liquid Reynolds numbers between 0.0277 and 5.55 with a corresponding gas Reynolds number ranging between 18.2 and 197. Characterizing the measured two-phase pressure drop in terms of the gas two-phase flow multiplier (ϕ_G^2) resulted in values between 1 and 1.44, where ϕ_G^2 increases with increasing superficial liquid velocity and decreases with increasing superficial gas velocity. Comparing the two-phase pressure drop predicted by several models showed the correlations for the separated flow model proposed by Lee and Lee [17] and Kim and Mudawar [16] predicted the experimental two-phase pressure with mean absolute percent errors ($|\bar{e}_{\%}|$) of 4.1% and 4.2%, respectively. Of the selected relative permeability models, the X-Model predicted the experimental data with a $|\bar{e}_{\%}|$ of 3.32%. Other homogeneous, separated, and relative permeability models produced a $|\bar{e}_{\%}|$ greater than 5%. The two-fluid model predicted the experimental two-phase pressure drop with a $|\bar{e}_{\%}|$ of 3.25% when using the new n_k value of 1.159 in the relative permeability.

The work also investigated the water film thickness. Imaging of the flow showed that the air-water experiments produced stratified flow for the range of test conditions. Measurements of the water film thickness show a decreasing trend with an increase in the ratio of air to water volumetric flow rate. The two-fluid model using $n_k = 1.159$ reasonably predicted the experimentally measured water film thickness with a mean error of −0.035, following the trend of the analytical solution of Steinbrenner [33]. Based on the analysis, the two-fluid model applies to thin microchannels for predicting both the two-phase pressure and the water film thickness.

Conflict of interest

The authors declare no conflict of interest for this work.

Acknowledgements

The authors gratefully acknowledge UCI's machinist, Ted Ediss, for his guidance in machining the microchannel assembly and Tuan Minh Nguyen for his help in setting up the imaging method. In addition, the authors thank Professor William A. Sirignano for his advice. Y. Wang thanks the Shanghai Everpower Technologies Ltd. for their partial financial support in PEM fuel cells.

Appendix A. Supplementary material

Supplementary data associated with this article can be found, in the online version, at https://doi.org/10.1016/j.ijheatmasstransfer.2018.08.060.

References

[1] X.C. Adroher, Y. Wang, Ex situ and modeling study of two-phase flow in a single channel of polymer electrolyte membrane fuel cells, J. Power Sources 196 (2011) 9544–9551, https://doi.org/10.1016/j.jpowsour.2011.07.076.
[2] M. Awad, Y. Muzychka, Effective property models for homogeneous two-phase flows, Exp. Therm. Fluid Sci. 33 (2008) 106–113, https://doi.org/10.1016/j.expthermflusci.2008.07.006.
[3] D. Beattie, P. Whalley, A simple two-phase frictional pressure drop calculation method, Int. J. Multiph. Flow 8 (1982) 83–87, https://doi.org/10.1016/0301-9322(82)90009-X.
[4] C.-Y. Chen, R.N. Horne, M. Fourar, Experimental study of liquid-gas flow structure effects on relative permeabilities in a fracture, Water Resour. Res. 40 (2004) 1–15, https://doi.org/10.1029/2004WR003026.
[5] E. Chinnov, F. Ron'shin, O. Kabov, Two-phase flow patterns in short horizontal rectangular microchannels, Int. J. Multiph. Flow 80 (2016) 57–68, https://doi.org/10.1016/j.ijmultiphaseflow.2015.11.006.
[6] D. Chisholm, A theoretical basis for the Lockhart-Martinelli correlation for two-phase flow, Int. J. Heat Mass Transfer 10 (1967) 1767–1778, https://doi.org/10.1016/0017-9310(67)90047-6.
[7] S.C. Cho, Y. Wang, Two-phase flow dynamics in a micro hydrophilic channel: a theoretical and experimental study, Int. J. Hear Mass Transfer 70 (2014) 340–352, https://doi.org/10.1016/j.ijheatmasstransfer.2013.11.003.
[8] A. Cicchitti, C. Lombardi, M. Silvestri, G. Soldaini, R. Zavattarelli, Two-phase cooling experiments: pressure drop, heat transfer and burnout measurements, Energia Nucl. 7 (1960) 407–425.
[9] A. Corey, The interrelation between gas and oil relative premeabilities, Producers Mon. 19 (1954) 38–41.
[10] A. Dukler, M. Wicks III, R. Cleveland, Frictional pressure drop in two-phase flow: B. An approach through similarity analysis, A.I.Ch.E J. 10 (1964) 44–51, https://doi.org/10.1002/aic.690100118.
[11] N.J. English, S.G. Kandlikar, An experimental investigation into the effect of surfactants on air-water two-phase flow in minichannels, Heat Transfer Eng. 27 (2006) 99–109, https://doi.org/10.1080/01457630500523980.
[12] M. Fourar, S. Bories, Experimental study of air-water two-phase flow through a fracture (narrow channel), Int. J. Multiph. Flow 21 (1995) 621–637, https://doi.org/10.1016/0301-9322(95)00005-I.
[13] M. Fourar, R. Lenormand, A viscous coupling model for relative permeabilities in a fracture, in: SPE Annual Technical Conference and Exhibition, September 27–30, Society of Petroleum Engineers, 1998, https://doi.org/10.2118/49006-MS.
[14] H. Huang, Z. Li, S. Liu, X.-y. Lu, Shan-and-chen-type multiphase lattice boltzmann study of viscous coupling effects for two-phase flow in porous media, Int. J. Numer. Meth. Fluids 61 (2009) 341–354, https://doi.org/10.1002/fld.1972.
[15] S. Kakac, R. Shah, W. Aung, Handbook of Single-Phase Convective Heat Transfer, Wiley, 1987.
[16] S.-M. Kim, I. Mudawar, Universal approach to predicting two-phase frictional pressure drop for adiabatic and condensing mini/micro-channel flows, Int. J. Heat Mass Transfer 55 (2012) 3246–3261, https://doi.org/10.1016/j.ijheatmasstransfer.2012.02.047.
[17] H.J. Lee, S.Y. Lee, Pressure drop correlations for two-phase flow within horizontal rectangular channels with small heights, Int. J. Multiph. Flow 27 (2001) 783–796, https://doi.org/10.1016/S0301-9322(00)00050-1.
[18] W. Li, Z. Wu, A general correlation for adiabatic two-phase pressure drop in micro/mini-channels, Int. J. Heat Mass Transfer 53 (2010) 2732–2739, https://doi.org/10.1016/j.ijheatmasstransfer.2010.02.029.
[19] X. Li, T. Hibiki, Frictional pressure drop correlation for two-phase flows in mini and micro single-channels, Int. J. Multiph. Flow 90 (2017) 29–45, https://doi.org/10.1016/j.ijmultiphaseflow.2016.12.003.
[20] S. Lin, C. Kwok, R.-Y. Li, Z.-H. Chen, Z.-Y. Chen, Local frictional pressure drop during vaporization of r-12 through capillary tubes, Int. J. Multiph. Flow 17 (1991) 95–102, https://doi.org/10.1016/0301-9322(91)90072-B.
[21] R. Lockhart, R. Martinelli, Proposed correlation of data for isothermal two-phase, two-component flow in pipes, Chem. Eng. Prog. 45 (1949) 39–48.
[22] Y. Ma, X. Ji, D. Wang, T. Fu, C. Zhu, Measurement and correlation of pressure drop for gas-liquid two-phase flow in rectangular microchannels, Chin. J. Chem. Eng. 18 (2010) 940–947, https://doi.org/10.1016/S1004-9541(09)60151-8.
[23] R. Martinelli, L. Boelter, T. Taylor, E. Thomsen, E. Morrin, Isothermal pressure drop for two-phase two-component flow in a horizontal pipe, Trans. A.S.M.E 66 (1944) 139–151.
[24] W. McAdams, W. Woods, I. Heroman Jr., Vaporization inside horizontal tubes–ii benzene-oil mixtures, Trans. A.S.M.E. 64 (1942) 193–200.
[25] K. Mishima, T. Hibiki, Some characteristics of air-water two-phase flow in small diameter vertical tubes, Int. J. Multiph. Flow 22 (1996) 703–712, https://doi.org/10.1016/0301-9322(96)00010-9.
[26] A. Nowamooz, G. Radilla, M. Fourar, Non-Darcian two-phase flow in a transparent replica of a rough-walled rock fracture, Water Resour. Res. 45 (2009) 1–9, https://doi.org/10.1029/2008WR007315.
[27] D. Pfund, D. Rector, A. Shekarriz, A. Popescu, J. Welty, Pressure drop measurements in a microchannel, AIChE J. 46 (2000) 1496–1507, https://doi.org/10.1002/aic.690460803.
[28] E. Romm, Fluid Flow in Fractured Rocks, Phillips Petroleum Co. [Translation of the 1966 version to English from Russian by William R. Blake], Bartlesville, Oklahoma, 1972.
[29] S. Saisorn, S. Wongwises, The effects of channel diameter on flow pattern, void fraction and pressure drop of two-phase airwater flow in circular microchannels, Exp. Therm. Fluid Sci. 34 (2010) 454–462, https://doi.org/10.1016/j.expthermflusci.2009.02.006.
[30] R. Shah, A correlation for laminar hydrodynamic entry length solutions for circular and noncircular ducts, J. Fluids Eng. 100 (1978) 177–179, https://doi.org/10.1115/1.3448626.
[31] R. Shah, A. London, Laminar Flow Forced Convection Heat Transfer and Flow Friction in Straight and Curved Ducts–A Summary of Analytical Solutions, Technical Report Standford University, Department of Mechanical Engineering, 1971.
[32] R. Shaw, The influence of hole dimensions on static pressure measurements, J. Fluid Mech. 7 (1960) 550–564, https://doi.org/10.1017/S0022112060000281.

[33] J.E. Steinbrenner, Two-phase Flow Phenomena in Fuel Cell Microchannels, Stanford University, 2011.
[34] L. Sun, K. Mishima, Evaluation analysis of prediction methods for two-phase flow pressure drop in mini-channels, Int. J. Multiph. Flow 35 (2009) 47–54, https://doi.org/10.1016/j.ijmultiphaseflow.2008.08.003.
[35] Y. Tang, D. Himmelblau, Velocity distribution for isothermal two-phase co-current laminar flow in a horizontal rectangular duct, Chem. Eng. Sci. 18 (1963) 143–148.
[36] Y. Wang, Porous-media flow fields for polymer electrolyte fuel cells ii. Analysis of channel two-phase flow, J. Electrochem. Soc. 156 (2009) B1134–B1141, https://doi.org/10.1149/1.3183785.
[37] Y. Wang, K.S. Chen, S.C. Cho, PEM Fuel Cells: Thermal and Water Management Fundamentals, Momentum Press, 2013.
[38] Y. Wang, K.S. Chen, J. Mishler, S.C. Cho, X.C. Adroher, A review of polymer electrolyte membrane fuel cells: technology, applications, and needs on fundamental research, Appl. Energy 88 (2011) 981–1007, https://doi.org/10.1016/j.apenergy.2010.09.030.
[39] W. Zhang, T. Hibiki, K. Mishima, Correlations of two-phase frictional pressure drop and void fraction in mini-channel, Int. J. Heat Mass Transfer 53 (2010) 453–465, https://doi.org/10.1016/j.ijheatmasstransfer.2009.09.011.